Korean J. Chem. Eng., 37(12), 2136-2142 (2020)
DOI: 10.1007/s11814-020-0670-7

pISSN: 0256-1115
eISSN: 1975-7220

Image cytometry of irregular microplastic particles in a cross-slot microchannel utilizing viscoelastic focusing

Bookun Kim*, Hwang Lee, Seong Jae Lee***,†, Jung-Hwan Kwon**,†, and Ju Min Kim*,****,†**

*Department of Energy Systems Research, Ajou University, Suwon 16499, Korea
**Division of Environmental Science and Ecological Engineering, Korea University, 145 Anam-ro, Seongbuk-gu, Seoul 02841, Korea
***Department of Polymer Engineering, The University of Suwon, Hwaseong, Gyeonggi 18323, Korea
****Department of Chemical Engineering, Ajou University, Suwon 16499, Korea
(*Received 20 May 2020 • Revised 19 August 2020 • Accepted 27 August 2020*)

Abstract−Microplastic particles have recently attracted much attention owing to their potential adverse effects on marine and terrestrial environments. Although several studies have been conducted on this topic, one of the prominent existing challenges is developing analytical methods to precisely characterize isolated microplastics. Specifically, a systematic method that determines both the size and shape of irregular micron-sized particles is required because conventional optical methods provide only two-dimensional images of microplastics and cannot easily handle cases of tilting or aggregation of particles. In this study, we demonstrate that previously developed microfluidic technologies can be successfully applied to measure the size and shape of oblate microparticles utilizing viscoelastic particle focusing. Furthermore, this technique is also applicable for irregular microplastic fragments that are predominantly found in environmental samples.

Keywords: Microplastic Particle, Cross-slot Microchannel, Viscoelastic Particle Focusing, Oblate-shape Particle, Extensional Flow

INTRODUCTION

Microplastics, typically defined as tiny plastic pieces of less than 5 mm length [1], have recently gained much attention owing to their potential threats to ecosystems and human health. Microplastics have been separated and identified in biota and in the environment in many recent studies, with the results showing that irregular fragments and fibers are dominant [2-7]. Although researchers have suspected that small and sharp-shaped microplastics have much stronger adverse effects than their large and spherical counterparts [8-10], characterizing the size and shape of microplastics using conventional optical methods (e.g., a microscope coupled with Fourier-transform infrared spectroscopy (FT-IR)) is an increasingly difficult task with the decreasing sizes of microplastics. Although analytical methods such as FT-IR and Raman spectroscopy can detect microplastics as small as 20 μm [11,12], spectroscopic identification does not meet the needs in the quantification of potentially more harmful microplastics in smaller size [13,14]. Scanning electron microscopy (SEM) [15,16] and thermal analysis [17] were also attempted, but they are also limited because of incomplete identification of plastics and destruction of samples. Thus, there is a growing need for analytical methods that can simultaneously characterize the sizes and shapes of microplastics in high throughput manner [18,19]. In addition, the microplastics found in various environments usually have irregular shapes, but systematic analyses of these shapes have not yet been developed.

Meanwhile, non-spherical ellipsoidal particles have been engineered for various applications such as interfacial rheology modifiers [20] or photonic crystals [21]. For example, it has been demonstrated that prolate ellipsoidal particles can be utilized to suppress the "coffee ring effect" typically observed during the drying process of particulate dispersion [20]. A strong network structure of the prolate particles is formed at the water-air interface by the capillary interactions between the particles, which renders the interface elastic. The coffee ring phenomenon, which is driven by the outward Deegan flow, is consequently suppressed owing to the elastic interface formed by the ellipsoidal particles. The interfacial rheology is affected by the shape of the ellipsoidal particles. On the other hand, oblate ellipsoidal particles can be used in a variety of applications such as secondary harmonic generation and surface-enhanced Raman scattering [22,23]. Therefore, the accurate shape measurements of these non-spherical particles will contribute to such practical applications [24].

The conventional method for measuring particle shape is to place the particle on a flat surface such as slide glass and then to observe it with optical microscopy or electron microscopy. Spherical particles can be easily observed and measured using such conventional methods. However, it is greatly challenging to measure the shapes of non-spherical particles, as these particles are not always

Electronic supplementary material The online version of this article (https://doi.org/10.1007/s11814-020-0670-7) contains supplementary material, which is available to authorized users.

†To whom correspondence should be addressed.
E-mail: sjlee@suwon.ac.kr, junghwankwon@korea.ac.kr, jumin@ajou.ac.kr

aligned in the same direction on a flat surface; instead, some particles may be tilted in out-of-plane direction [24-27]. Furthermore, non-spherical particles are often found in out-of-focus planes and tend to aggregate into clusters [28]. These problems complicate the accurate measurements of the shapes of non-spherical particles. It has been demonstrated that the prolate ellipsoidal particles are constantly aligned along the extensional principal axis at the central stagnation point of a microfluidic cross-slot channel [24]. In addition, these particles are focused along the channel centerline in a polymer solution through the viscoelastic particle migration mechanism while moving from an inlet to the stagnation point. In this work, we demonstrate that the previously developed microfluidic technologies can be applied to the shape measurements for oblate particles and also irregular particles mimicking microplastics.

METHODOLOGY

1. Microchannel Geometry and Fabrication

A schematic illustration of the cross-slot channel is presented in Fig. 1. The square cross section is composed of width (w)×height (h)=50 μm×50 μm. The four-walled polydimethylsiloxane (PDMS) microchannel was fabricated following conventional soft lithography [31]. The prepolymer base and curing agent of PDMS (10 : 1) (Sylgard 184, Dow) were thoroughly mixed and then degassed in a vacuum chamber (≈30 min). The mixture was poured onto the silicon master mold that included the microchannel geometry. Both PDMS channel and slab were cured at 65 °C for 6 h and then the silicon wafers were peeled off. Holes for both the inlet and outlet were made with a punch (World Precision Instruments, 0.75 mm diameter). The PDMS was cut to the size of a slide glass and then placed atop it. Both PDMS surfaces (microchannel geometry and the flat slab) were placed in an air plasma chamber (PDC-32G, Harrick) at 250 mTorr for 2 min, and subsequently the surfaces of the PDMS channel and the slab exposed to the air plasma were immediately contacted to covalently bond with each other. Hard baking was performed for 2 h at 180 °C to totally remove the solvent and to strengthen the covalent bond.

2. Materials and Image Acquisition

We prepared a 6.8 wt% polyvinylpyrrolidone [PVP; Sigma-Aldrich (MW=360,000 g/mol)] aqueous solution in deionized water

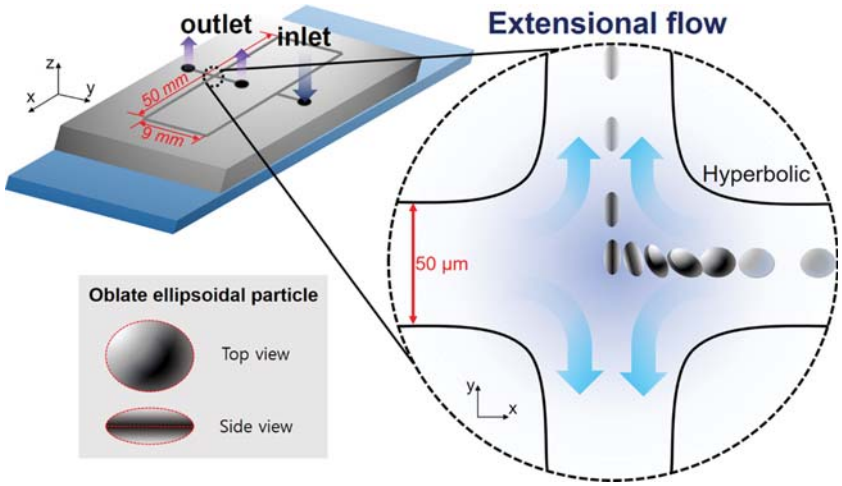

Fig. 1. Schematic diagram for the spatially focused and orientationally aligned oblate ellipsoidal particles under the viscoelastic flow in a cross-slot microchannel, which generates the strong extensional stress field as shown in the inset.

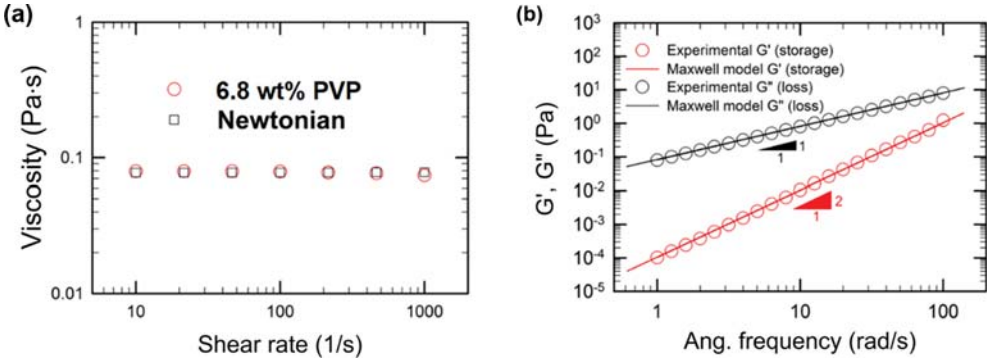

Fig. 2. Rheological properties of the viscoelastic 6.8 wt% polyvinylpyrrolidone (PVP) and Newtonian 24.7 wt% dextran aqueous solutions, which were measured at 20 °C with a rotational rheometer [cone and plate (60 mm); AR-G2, TA-instruments]. Each datum point was obtained by averaging three data points. (a) Steady shear viscosities of the Newtonian and viscoelastic fluids. (b) Storage (G′) and loss (G″) moduli, and theoretical predictions (solid lines) using upper-convected Maxwell model.

as a viscoelastic fluid. Additionally, we prepared a Newtonian fluid with 24.7 wt% dextran [Sigma-Aldrich (MW=40,000 g/mol)] solution in deionized water. The rheological properties of both solutions are provided in Fig. 2. Micron-sized microplastic and oblate ellipsoidal particles were flowed into the microchannel through a single inlet with a syringe pump (11 Plus, Harvard Apparatus). Oblate ellipsoidal polystyrene (PS) beads were made from spherical beads with 5 μm diameter using the film squeezing process [32]. A PS petri dish (SPL Life Sciences, Korea) was sawed to collect debris, which was then followed by sieving (pore size: 50 μm). The sieved PS particles were suspended in water for 20 min, and then the PS particles in the supernatant were collected. 0.01 vol% TWEEN 20 (Sigma-Aldrich) was added to the particle-laden solutions to prevent the aggregation of the particles. A high-speed camera (MC2, Photron) mounted on an inverted optical microscope (IX71, Olympus) was used to capture movies. A 60× objective lens was used to observe oblate ellipsoidal particles with additional internal 1.6× magnification, and a 20× lens was also used for the experiments of irregular particles prepared from the sawed PS petri dish. We excluded small particles of which the short axis lengths were shorter than 4 μm and the measurement accuracy was estimated to be 625 nm (=distance per pixel), when the shapes of irregular particles were measured. All the movies were captured at 3,000 frames per second (fps) with shutter speeds ranging from 1/10,000 to 1/20,000 s. All the images were processed with ImageJ software (NIH). SEM images were acquired with a nano pattern generation system (SEM-NPGS, JSM-6380).

RESULTS AND DISCUSSION

In this experiment, we employed a cross-slot microfluidic device to measure the shapes of non-spherical particles; a schematic diagram of the microchannel is presented in Fig. 1. We used the same cross-slot channel with hyperbolic-shaped walls as used in the previous studies [24,29,30]. In the cross-slot microchannel, the particle-laden solution is injected through one inlet and its fluid stream is divided into two equivalently branched channels. The two fluid streams meet again at the cross-slot region as shown in Fig. 1. The particles suspended in the medium experience the planar extensional flow field at the stagnation point (center) of the cross-slot channel. The cross-slot microchannel has been widely used to generate the planar extensional flow field in studying cell mechanics and polymer physics [30,33,34]. Particles simultaneously experience both compression along the inlet direction and extension along the outlet direction in the planar extensional flow field (Fig. 1). A previous study demonstrated that the planar extensional flow field at the cross-slot self-aligns an prolate ellipsoidal particle along the extensional principal axis [24]. The particle alignment in the cross-slot channel was harnessed to accurately measure the shapes of the prolate particles [22]. However, it is still unclear whether the particle shape measurements based on the cross-slot channel can be applied to the non-spherical particles other than the prolate shape. In this study, we observed that oblate ellipsoidal and irregular particles are also aligned in the planar extensional flow field, which was engineered for their shape measurements.

Meanwhile, the particles at the inlet are randomly distributed in the channel cross-section if the particles are suspended in Newtonian fluid at low Reynolds number (Re) conditions. Therefore, only a very small number of particles are expected to reach the stagnation point, which deteriorates the measurement efficiency. It has been previously demonstrated that the measurement efficiency can be significantly enhanced by focusing particles along the channel centerline in a viscoelastic fluid, which was also employed in this study. We tested two different particle-suspending media: Newtonian (24.7 wt% dextran aqueous solution) and viscoelastic (6.8 wt% PVP aqueous solution) fluids. The measured shear viscosity of the Newtonian fluid was 77 cP, which closely matched that of the viscoelastic fluid (78 cP) [Fig. 2(a)]. The elastic nature of the viscoelastic fluid was typically characterized with its relaxation time (λ) and measured with the small amplitude oscillatory shear (SAOS) test as shown in Fig. 2(b). The relaxation time (λ) was measured to be 1.4 ms using an upper-convected Maxwell model [35]. The viscoelastic nature is usually characterized with the Weissenberg number [$Wi=\lambda\dot{\varepsilon}_c=\lambda(U/D)=(2\lambda Q/hw^2)$], which denotes the relative ratio of elastic to viscous forces. $\dot{\varepsilon}_c$ is the characteristic strain rate defined by U/D, where U is the characteristic velocity (=Q/hw), D is the characteristic length scale (=h/2), Q is the volumetric flow rate, and h and w are the channel height and width, respectively [36,37].

The spherical particles laterally migrate by the imbalanced first and second normal stress differences (N_1 and N_2) in the pressure-driven flow of the viscoelastic fluid, which was theoretically predicted with second-order fluid and also experimentally observed [38-41]. In the polymer solutions, the magnitude of the second normal stress difference ($N_2=\tau_{22}-\tau_{33}$) was significantly smaller than that of the first normal stress difference ($N_1=\tau_{11}-\tau_{22}$) [35,41], where τ_{11}, τ_{22}, and τ_{33} are the normal stresses in the directions of velocity, velocity gradient, and vorticity, respectively. When the viscoelastic fluid is modeled using the upper-convected Maxwell model, the first normal stress difference can be denoted as $N_1=2\lambda\mu_0\dot{\gamma}^2$ in the pressure-driven channel flow (μ_0: solution viscosity, $\dot{\gamma}$: local shear rate) [35]. The elastic force (F_E) exerted on a spherical particle can be semi-empirically modelled as $F_E\sim a^3\nabla N_1$ [35,41,42], where a is the particle radius. Therefore, the particles migrate toward the low shear rate regions at the channel centerline or four corners in a square channel [38,39]. The particles in the viscoelastic fluid can be also affected by the inertial force, which is characterized by Re; this number is defined as $Re=2Q\rho/(w+h)\mu_0$ (ρ: fluid density), which denotes the relative ratio of inertial to viscous forces. However, the inertial particle migration can be neglected in this study because the Re values were exceedingly small for all current experimental conditions (<0.1). In addition, the lateral particle motion by the shear-induced migration arising from particle-particle interaction [43,44] was also negligible because the particle volume fraction was as low as ~0.01. Consequently, we can conclude that the lateral migration and focusing of oblate ellipsoidal and irregular particles observed in the viscoelastic fluid (PVP aqueous solution) were driven by the gradient of N_1. It was demonstrated that the particle focusing along the channel centerline significantly enhances the measurement efficiency when the cross-slot channel is used for the shape measurement of the prolate particles [24].

As shown in Fig. 3(b), we measured the shape of the particles

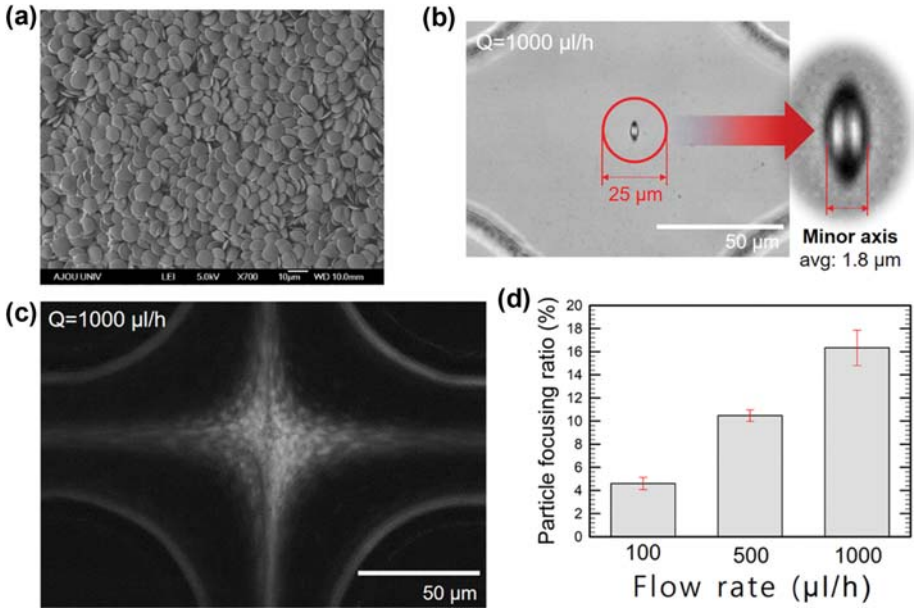

Fig. 3. (a) Scanning electron microscope (SEM) image of oblate ellipsoidal particles. (b) The orientation of the particles is aligned along the outlet direction in the cross-slot region, and the sizes and shapes of the particles, which are spatially focused and orientationally aligned, are measured. The particle size was measured when a particle passed the red-circled region (diameter=25 μm), in which the flow kinematics was homogeneous [29,54]. (c) Z-projection image stacked with the "standard deviation" option in ImageJ software at a flow rate of 1,000 μl/h. (d) Focusing efficiency (F.E.) according to flow rates when a particle passes the red-circled region.

entering the red-circled zone (diameter=25 μm) at the center of the cross-slot channel [45]; this red-circled region, with uniform strain rate and flow characteristics, was selected as per the specifications of previous studies [24,29,30]. The relative ratio of the particles passing through the red-circled zone to all particles is defined by the "focusing efficiency" (F.E.). In the previous studies, the dimensionless lateral migration velocity (v/U) for both spherical and prolate ellipsoidal particles increased with increasing to Wi, which denotes that particles are more tightly focused along the channel centerline when increasing the flow rate [24,39,40]. This enhanced particle focusing was also observed for the current oblate ellipsoidal particle case: F.E. increased as the flow rate gradually increased from Q=100 μl/h (F.E.=5%, Wi=0.15) to 1,000 μl/h (F.E.=16%, Wi=1.5) as shown in Fig. 3(d). In addition, a large number of particles were distributed near the center of the cross-slot as shown with the standard deviation image (3000 stacked images, 6.8 wt% PVP solution, Q=1,000 μl/h) in Fig. 3(c), confirming the focusing of the oblate particles along the channel centerline. For comparison, the oblate ellipsoidal particles suspended in the Newtonian fluid (24.7 wt% dextran solution) were also tested; however, we could not find any particles that reached the red-circled zone on the focal plane at the flow rate of Q=1,000 μl/h (n=500).

In our previous study, the shapes of prolate ellipsoidal particles were measured in the extensional flow of the cross-slot channel [24], where the long axis direction of the prolate ellipsoidal particles was aligned parallel to the outlet direction at the stagnation point. In contrast, the oblate ellipsoidal particles, which look much like "go stones," have a wide area when viewed from above but a narrow area viewed from the side, as shown in Fig. 1. Therefore, it is challenging to measure the length of the side to determine the overall shape because the oblate ellipsoidal particle cannot be easily aligned for accurate side-view observations. However, it was theoretically predicted that these oblate ellipsoidal particles are aligned to show the side in extensional flow field when viewed from above [46]. Therefore, the oblate ellipsoidal particle is expected to self-align to show the side as perpendicular to the outlet direction in the cross-slot channel, as shown in Fig. 1. Therefore, we conclude that the particles rotate at the stagnation point only through the pure planar extensional flow field, which is consistent with the previous theoretical prediction [46]. The oblate ellipsoidal particles cannot be easily measured with conventional methods such as SEM, as shown in Fig. 3(a). Most particles irregularly lie on the plate, and the sides of the particles are difficult to locate for their length measurement. In addition, it is difficult to obtain an accurate outline of the top surface because of the overlapping of the particles and the tilting of the particles in an out-of-plane direction in a similar way to the prolate ellipsoidal particles [24]. We used the cross-slot microfluidic device to overcome the disadvantages of the traditional optical methods following the previous approach [24]. The accurate measurement of the oblate ellipsoidal particle was enabled by the self-alignment in the cross-slot microchannel to show the side of the particle, as shown in Fig. 3(b). In addition, to our knowledge, these experimental results are the first to corroborate the previous theoretical prediction on the alignment of the oblate ellipsoidal particles in the extensional flow field [46]. In Fig. 3(b) [also refer to Movie S1], the measured length of the short axis (side length) was 1.8±0.1 μm (n=200) for the current oblate ellipsoidal particle case. The current experimental results show that the shape information measured in the cross-slot microfluidic device can be used to supplement their corresponding data

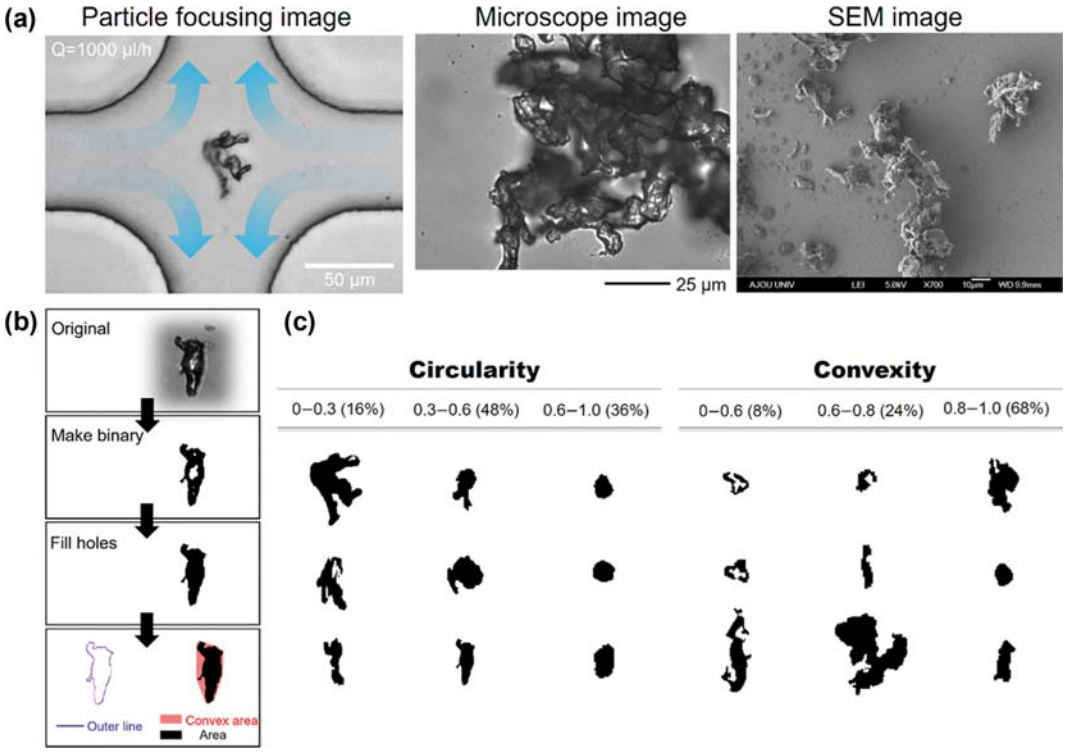

Fig. 4. (a) Representative image for a spatially focused and orientationally aligned microplastic particle (left); optical microscope image (middle) and scanning electron microscope (SEM) image for microplastic particles (right). (b) Circularity and convexity measurement procedures using ImageJ software. (c) Representative binary images for irregular microplastic particles and their probability distributions according to circularity and convexity (n=200).

obtained with the conventional optical methods. Consequently, the current experimental data along with the previous results of the prolate ellipsoidal particles [24] demonstrate that it is possible to apply the microfluidics-based approach to measure the shapes of various non-spherical particles, including irregular particles.

Microplastics have recently emerged as a major environmental problem, and their shapes are usually irregular because of weathering [48]. The cross-slot microchannel was applied to measure the shape of irregular microplastic particles. To mimic the fine dust particles in the environment, the particles collected from sawed polystyrene (PS) petri dishes (refer to the Experimental section) were considered in this study. We followed the same procedures as the oblate ellipsoidal particle case to measure the shapes of the irregular particles. The optical images obtained by conventional optical microscopy (not relying on the microfluidic device) and SEM [Fig. 4(a)] have similar problems as those of the oblate ellipsoidal particle [Fig. 3(a)]; the particles are tilted out-of-plate and are placed on the out-of-focusing plane [22]. In addition, it is difficult to distinguish clear outlines because of the overlapping of the particles [22]. However, it is expected that the aggregated particles are separated in the extensional flow field in a similar manner as the previous study [49], which enables individual particle analysis (refer to Movie S2). Furthermore, we measured the shapes of the irregular particles with the alignment of the long axis at the stagnation point of the cross-slot channel (we measured the shape of each irregular particle when the particle center entered the red-circled region.

We added additional image post-processing steps because the fine microplastic particles had irregular shapes. As shown in Fig. 4(b), we converted the original images to black and white images with the "binary option" of the ImageJ software, and then applied the "fill holes option" to fill the empty spaces of the particle images. For the current sample, the measured lengths of the long and short axes were 11.7±3.8 μm (n=200) and 6.1±2.4 μm (n=200), respectively, and the corresponding aspect ratio (AR) was approximately 1.9. When the particle size was characterized with an equivalent circle diameter, it was 8.8±3 μm. The equivalent circle diameter of an irregular particle is defined by the diameter of the circle, when the area of an irregular particle is converted to that of a circle. The irregularity of the particles is prominently characterized with circularity and convexity as shown in Fig. 4(c); circularity and convexity are frequently used to extract the morphological characteristics for irregular particles [50]. In this study, the circularity is defined as $\sqrt{4\pi A/p^2}$, where p is the outer line of the particle and A is the particle area; the convexity is defined as particle area/convex area [51,52]. The convex area is the area surrounding the branches protruding outward from the particles [refer to Fig. 4(b)]. The largest portion of the measured circularity of the model microplastic sample (48%) was in the range of 0.3-0.6, and 68% of the convexity was between 0.8-1.0. Circularity is used to denote how close a particle is to a circle [53]. The current results show that the shapes of many irregular particles (circularity: 0.3-0.6) depart from the circle (circularity ~1) [also refer to Fig. 4(c)]. In contrast, the convexity data (0.8-1.0) of many particles denote that there are few branches protruding around the particles [Fig. 4(c)] [38,39]. In

conclusion, most particles in the sample are non-spherical shapes with few branches around them.

CONCLUSIONS

We applied the microfluidic method to measure the shape of non-spherical particles using the particle alignment in an extensional flow field combined with viscoelastic particle focusing [24, 29,30]. We demonstrated that the oblate ellipsoidal particles are self-aligned to show their sides in the extensional flow fields, which is consistent with the previous theoretical prediction. Based on this observation, we demonstrated that the short-axis lengths of oblate ellipsoidal particles can be successfully measured, overcoming the out-of-focus and particle tilting problems that are common when used with traditional methods. Furthermore, we applied the current method to characterize the shapes of the irregular particles that could not be defined with ellipsoidal shapes. The current experimental results show that the cross-slot microdevice-based approach can be applied to various non-spherical particle analysis tools. Finally, we expect that the current method can be used collect to morphological data of micro-particles related to global environmental issues, such as atmospheric fine dust and marine microplastic pollution.

ACKNOWLEDGEMENTS

This research was supported by the Research Program through the National Research Foundation of Korea (NRF) (nos. NRF-2019R1F1A1060512, NRF-2018R1A5A1024127, and 2020R1A2C2009244).

REFERENCES

1. C. J. Moore, *Environ. Res.*, **108**, 131 (2008).
2. M. A. Browne, P. Crump, S. J. Niven, E. Teuten, A. Tonkin, T. Galloway and R. Thompson, *Environ. Sci. Technol.*, **45**, 9175 (2011).
3. S. M. Ehlers and J. A. Ellrich, *Mar. Pollut. Bull.*, **151**, 110845 (2020).
4. H. Leslie, S. Brandsma, M. Van Velzen and A. Vethaak, *Environ. Int.*, **101**, 133 (2017).
5. T. Lim, G. Y. Jung, J. H. Kim, S. O. Park, J. Park, Y. T. Kim, S. J. Kang, H. Y. Jeong, S. K. Kwak and S. H. Joo, *Nat. Commun.*, **11**, 1 (2020).
6. H. Park, M. J. Oh, P. G. Kim, G. Kim, D. H. Jeong, B. K. Ju, W. S. Lee, H. M. Chung, H. J. Kang and J. H. Kwon, *Environ. Sci. Technol.*, **54**, 1503 (2020).
7. M. Scheurer and M. Bigalke, *Environ. Sci. Technol.*, **52**, 3591 (2018).
8. J. S. Choi, Y.-J. Jung, N.-H. Hong, S. H. Hong and J.-W. Park, *Mar. Pollut. Bull*, **129**, 231 (2018).
9. A. D. Gray and J. E. Weinstein, *Environ. Toxicol. Chem.*, **36**, 3074 (2017).
10. S. L. Wright, R. C. Thompson and T. S. Galloway, *Environ. Pollut.*, **178**, 483 (2013).
11. S. Eo, S. H. Hong, Y. K. Song, J. Lee, J. Lee and W. J. *Shim, Environ. Pollut.*, **238**, 894 (2018).
12. M. Bergmann, L. Gutow and M. Klages, *Marine anthropogenic litter*, Springer, New York (2015).
13. H. Bouwmeester, P. C. Hollman and R. J. Peters, *Environ. Sci. Technol.*, **49**, 8932 (2015).
14. L. G. A. Barboza, C. Lopes, P. Oliveira, F. Bessa, V. Otero, B. Henriques, J. Raimundo, M. Caetano, C. Vale and L. Guilhermino, *Sci. Total Environ.*, **717**, 134625 (2020).
15. L. M. Hernandez, E. G. Xu, H. C. Larsson, R. Tahara, V. B. Maisuria and N. Tufenkji, *Environ. Sci. Technol.*, **53**, 12300 (2019).
16. A. Naji, M. Nuri and A. D. Vethaak, *Environ. Pollut.*, **235**, 113 (2018).
17. E. Fries, J. H. Dekiff, J. Willmeyer, M.-T. Nuelle, M. Ebert and D. Remy, *Environ. Sci. Process. Impacts*, **15**, 1949 (2013).
18. W. J. Shim, S. H. Hong and S. E. Eo, *Anal. Methods*, **9**, 1384 (2017).
19. S. Zhang, J. Wang, X. Liu, F. Qu, X. Wang, X. Wang, Y. Li and Y. Sun, *Trends Anal. Chem.*, **111**, 62 (2019).
20. P. J. Yunker, T. Still, M. A. Lohr and A. Yodh, *Nature*, **476**, 308 (2011).
21. T. Ding, K. Song, K. Clays and C. H. Tung, *Adv. Mater.*, **21**, 1936 (2009).
22. A. Wokaun, J. Bergman, J. Heritage, A. Glass, P. Liao and D. Olson, *Phys. Rev. B*, **24**, 849 (1981).
23. P. Royer, J. L. Bijeon, J. P. Goudonnet, T. Inagaki and E. T. Arakawa, *Surf. Sci.*, **217**(1-2), 384 (1989).
24. J. Kim, J. Y. Kim, Y. Kim, S. J. Lee and J. M. Kim, *Anal. Chem.*, **89**, 8662 (2017).
25. J. Li, Y. Wei, Y. Deng, D. Gu, X. Yang, L. Zhang, B. Tu and D. Zhao, *J. Mater. Chem.*, **20**, 6460 (2010).
26. D. Li and Y. Wang, *Plasmonic nanostructures as surfaceenhanced Raman scattering (SERS) substrate for protein biomarker sensing*, InTech, London (2017).
27. A. Mazzoli and O. Favoni, *Powder Technol.*, **225**, 65 (2012).
28. G. Batchelor, *J. Fluid Mech.*, **46**, 813 (1971).
29. S. Cha, T. Shin, S. S. Lee, W. Shim, G. Lee, S. J. Lee, Y. Kim and J. M. Kim, *Anal. Chem.*, **84**, 10471 (2012).
30. Y. B. Bae, H. K. Jang, T. H. Shin, G. Phukan, T. T. Tran, G. Lee, W. R. Hwang and J. M. Kim, *Lab Chip*, **16**, 96 (2016).
31. Y. Xia and G. M. Whitesides, *Annu. Rev. Mater. Sci.*, **28**, 153 (1998).
32. S. J. Ahn, K. H. Ahn and S. J. Lee, *Colloid Polym. Sci.*, **294**, 859 (2016).
33. G. B. Jeffery, *Proc. R. Soc. Lond.*, **102**, 161 (1922).
34. C. J. Petrie, *J. Non-Newton. Fluid Mech.*, **87**, 369 (1999).
35. R. B. Bird, R. C. Armstrong and O. Hassager, *Dynamics of polymeric fluids fluid mechanics*, Wiley Interscience, New York (1987).
36. L. Rodd, J. Cooper-White, D. Boger and G. H. McKinley, *J. Non-Newton. Fluid Mech.*, **143**, 170 (2007).
37. L. E. Rodd, T. P. Scott, D. V. Boger, J. J. Cooper-White and G. H. McKinley, *J. Non-Newton. Fluid Mech.*, **129**, 1 (2005).
38. B. Ho and L. Leal, *J. Fluid Mech.*, **76**, 783 (1976).
39. S. Yang, J. Y. Kim, S. J. Lee, S. S. Lee and J. M. Kim, *Lab Chip*, **11**, 266 (2011).
40. B. Kim and J. M. Kim, *Biomicrofluidics*, **10**, 024111 (2016).
41. A. M. Leshansky, A. Bransky, N. Korin and U. Dinnar, *Phys. Rev. Lett.*, **98**, 234501 (2007).
42. M. Tehrani, *J. Rheol.*, **40**, 1057 (1996).
43. M. Han, C. Kim, M. Kim and S. Lee, *J. Rheol.*, **43**, 1157 (1999).
44. D. Leighton and A. Acrivos, *J. Fluid Mech.*, **181**, 415 (1987).
45. R. Dylla-Spears, J. E. Townsend, L. Jen-Jacobson, L. L. Sohn and S. J. Muller, *Lab Chip*, **10**, 1543 (2010).
46. W. R. Schowalter, A. Luikov and W. Minkowycz, *Progress in heat*

and mass transfer: Selected papers of the 1970 international seminar, Elsevier, New York (2013).
47. E. Guazzelli and J. F. Morris, *A physical introduction to suspension dynamics*, Cambridge University Press, New York (2011).
48. A. Jahnke, H. P. H. Arp, B. I. Escher, B. Gewert, E. Gorokhova, D. Kühnel, M. Ogonowski, A. Potthoff, C. Rummel and M. Schmitt-Jansen, *Environ. Sci. Technol. Lett.*, **4**, 85 (2017).
49. Y. Kim, K. H. Ahn and S. J. Lee, *J. Membr. Sci.*, **534**, 25 (2017).
50. I. Kursun, *Min. Proc. Ext. Met. Rev.*, **30**, 346 (2009).
51. C. Mora and A. Kwan, *Ceme. Concr. Res.*, **30**, 351 (2000).
52. W. C. Krumbein, *J. Sediment. Res.*, **11**, 64 (1941).
53. E. Olson, *J. GXP Compliance*, **15**, 85 (2011).
54. D. R. Gossett, T. Henry, S. A. Lee, Y. Ying, A. G. Lindgren, O. O. Yang, J. Rao, A. T. Clark and D. Di Carlo, *Proc. Natl. Acad. Sci. U.S.A.*, **109**, 7630 (2012).